

## Direct detection of linearized bursts in turbulence

Javier Jiménez

Citation: [Physics of Fluids \(1994-present\)](#) **27**, 065102 (2015); doi: 10.1063/1.4921748

View online: <http://dx.doi.org/10.1063/1.4921748>

View Table of Contents: <http://scitation.aip.org/content/aip/journal/pof2/27/6?ver=pdfcov>

Published by the [AIP Publishing](#)

---

### Articles you may be interested in

[Experimental study of spectral energy fluxes in turbulence generated by a fractal, tree-like object](#)  
Phys. Fluids **25**, 110810 (2013); 10.1063/1.4819351

[How linear is wall-bounded turbulence?](#)

Phys. Fluids **25**, 110814 (2013); 10.1063/1.4819081

[Direct numerical simulation of an isothermal reacting turbulent wall-jet](#)

Phys. Fluids **23**, 085104 (2011); 10.1063/1.3622774

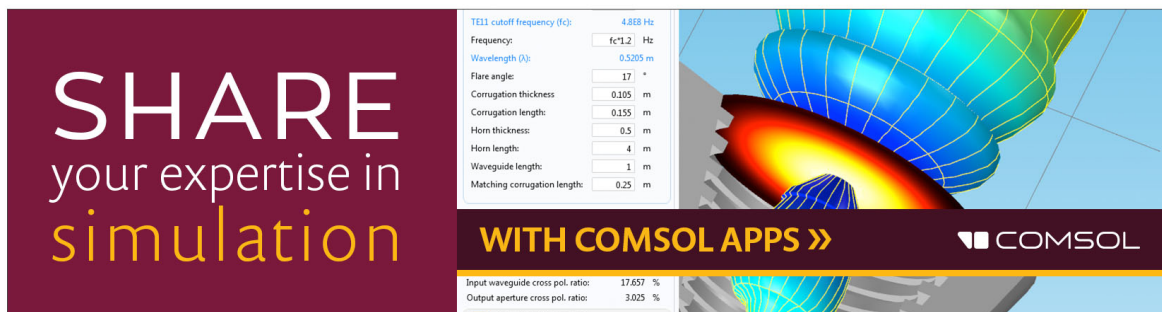
[Characterization of near-wall turbulence in terms of equilibrium and “bursting” solutions](#)

Phys. Fluids **17**, 015105 (2005); 10.1063/1.1825451

[On the comparison of turbulence intensities from large-eddy simulation with those from experiment or direct numerical simulation](#)

Phys. Fluids **14**, 1809 (2002); 10.1063/1.1466824

---



**SHARE**  
your expertise in  
**simulation**

TE11 cutoff frequency (fc): 4.888 Hz  
Frequency:  $fc \times 1.2$  Hz  
Wavelength ( $\lambda$ ): 0.5205 m  
Flare angle: 17 °  
Corrugation thickness: 0.105 m  
Corrugation length: 0.155 m  
Horn thickness: 0.5 m  
Horn length: 4 m  
Waveguide length: 1 m  
Matching corrugation length: 0.25 m

**WITH COMSOL APPS »**

COMSOL

Input waveguide cross pol. ratio: 17.657 %  
Output aperture cross pol. ratio: 3.025 %  
 Target criterion: passed

## Direct detection of linearized bursts in turbulence

Javier Jiménez

*School of Aeronautics, Universidad Politécnica de Madrid, 28040 Madrid, Spain*

(Received 19 January 2015; accepted 14 May 2015; published online 2 June 2015)

The relevance of linear transitional mechanisms in fully turbulent shear flows, and in particular of the Orr-like inviscid transient amplification of disturbances, is explored in the context of the prediction of bursting behavior. Although the logarithmic layer of wall-bounded turbulence is used as the primary example, most conclusions should apply to other flows with linearly stable mean profiles that are dominated by large-scale streamwise-velocity streaks and intermittent bursts of the cross-shear velocity. When the linearised problem is solved in the limit of small viscosity, it has previously been shown that statistical properties, such as the bursting time- and length-scales, the energy fluxes between components, and the mean inclination angles, are consistent in linear and nonlinear systems. The question addressed here is whether the individual structures predicted by the linearised solution can be detected in fully nonlinear simulations, and whether the linearized approximation can be used to predict their evolution. It is found that strong bursting of the largest scales is well described linearly, comprising about 65%–70% of the total time, but that weaker fluctuations are not. It is also found that adding an eddy viscosity does not substantially improve predictions. © 2015 AIP Publishing LLC. [<http://dx.doi.org/10.1063/1.4921748>]

### I. INTRODUCTION

Turbulence is a nonlinear phenomenon. Linear autonomous model cannot determine the magnitude of the turbulent intensities, and it is difficult to imagine how a multiscale cascade<sup>1</sup> may be modeled linearly. On the other hand, some particular aspects of shear turbulence are well described by linear approximations, particularly the energy-production mechanism of the largest flow scales. The ultimate energy source in a shear flow is the velocity difference across the mean profile, and the interaction of the mean shear with the fluctuations, rather than of the fluctuations with each other, can be used as an effective definition of linearity. The best-known example is the Kelvin–Helmholtz instability of mean velocity profiles with inflection points, which controls many properties of the large-scale structures of fully turbulent free-shear flows.<sup>2</sup> The focus of this paper is the behavior of wall-bounded flows, whose mean profile typically lacks inflection points and is linearly stable.<sup>3</sup> Even in that case, it has been known for some time that the “lift-up” of the mean velocity profile by the cross-shear velocity,  $v$ , is one of the dominant mechanisms for the production of turbulent energy,<sup>4–7</sup> and is contained in the linearized equations.<sup>8,9</sup>

The result of the lift-up is the formation of the streamwise-velocity streaks that dominate the kinetic energy of wall-bounded flows. There is less consensus about the generation of the required fluctuations of  $v$ , which take the form of intermittent bursts.<sup>10–12</sup> The prevailing theory is that their energy is drawn from the perturbation velocity of strong streaks,<sup>13</sup> in a process that, even if often presented as a linear streak instability, depends on a finite streak amplitude and is therefore nonlinear. It is known that streaks are required for the generation of  $v$ , in the sense that artificially damping them prevents the generation of new  $v$  structures.<sup>14</sup> However, while this clarifies how bursts are initiated, we will be more interested in their subsequent evolution, and on the source of the energy required for their intensification. Reference 7 argued that the streak-driven model does not explain the mismatch between the temporal and spatial scales of the long-lived streaks and of the shorter-lived  $v$  bursts. It is furthermore unclear how the streaks survive after transferring their energy to the bursts.<sup>15</sup> A key breakthrough was the realization that even linearly stable perturbations can “transiently” extract energy directly from the mean flow,<sup>5,16,17</sup> and thus give rise

to transient bursts. The hypothesis that we test in this paper is that the bursts in wall-bounded turbulence are basically Orr-like events<sup>18</sup> in which the transient amplification of the wall-normal velocity is the result of the tilting of the structures by the mean shear.<sup>7</sup> This is an inviscid process in which energy is drawn directly by the perturbation from the mean velocity profile. As such, it can be considered linear in the sense explained above, even when finite amplitudes are involved. Inviscid Orr bursts have lifetimes of the order of the inverse of the mean shear. They eventually return to the mean flow the energy that they have previously borrowed from the mean flow during the first part of the burst. But they are relevant to the overall energy balance because they couple with the mean velocity profile to generate longer-lived streamwise velocity streaks that only decay dissipatively.

The previously cited references have established that some statistical properties of wall-bounded flows are consistent with the predictions of linear models. For example, the most amplified linear perturbations of the mean velocity profiles of turbulent channels are similar in dimensions and geometry to the structures observed in real turbulent flows,<sup>5,6</sup> and so are their bursting period and the temporal correlations between the different flow variables.<sup>7,19</sup> However, although these results are highly suggestive, it is still possible that they may only reflect statistical averages that are seldom observed in the flow, or that they hide intermittent events that are nevertheless important for the flow dynamics. Here, we will be interested in going beyond bulk statistics and correlations, and into the properties of individual events. In particular, we will inquire whether the behavior predicted by linear models can be identified in fully nonlinear turbulent channels. We will quantify how closely and how often the flow approaches those models, and explore whether they can be used to predict the flow behavior at least part of the time. Note that the latter, by itself, would be a useful tool in flow control.

The ultimate aim of such a program should be the identification and tracking of short-lived structures in full-scale flows, but this remains a long-term goal. The first steps were taken some time ago with the characterization of structures as localized regions in which some flow property is particularly strong,<sup>15,20,21</sup> in the spirit of the classical quadrant analysis of sweeps and ejections.<sup>22,23</sup> These objects were then tracked in time, although their interactions, mergers, and splits complicate their temporal coherence.<sup>24</sup> The results provide inestimable information on the kinematics of the flow, but are difficult to relate to the equations of motion. A more “analytic” approach, although still kinematic, is the use of simulations in minimal domains that are small enough to contain single structures of some particular kind.<sup>10,12</sup> These domains avoid the problem of structure segmentation, because the evolution of the flow can be studied by the box-wide integrals of relevant quantities. It was found in this way that the properties of the  $v$ -bursts are approximately the same in minimal channels,<sup>11,12</sup> segmented structures of large channels,<sup>24</sup> and equilibrium homogeneous shear turbulence,<sup>7,19</sup> strongly suggesting that bursts are general features of shear flows.

Since box averaging is a simple linear operation, it is possible to write equations for its evolution and for its wall-normal structure. Unfortunately, such equations are unlikely to be closed, because the equations of motion require horizontal gradients that are hidden by the averaging. For example, the tilting mentioned above for Orr bursts cannot be defined for functions that depend exclusively on  $y$ . It is usually necessary to include some of the wall-parallel structure of the flow field, and the next simplest characterization beyond averaging is expansion into individual Fourier modes.<sup>7</sup> Here, we will use time-resolved direct simulations of turbulent channels in relatively small periodic boxes in which the first few wall-parallel Fourier harmonics are taken to represent the behavior of individual structures. The detailed reasoning behind this choice is deferred to Sec. II.

The organization of this paper is as follows. Section II introduces the theoretical model to be tested, the equations of motion, and the choice of variables. Section III describes the numerical data sets. Section IV reports the results of using different linear models to predict the evolution of the chosen variables, and Sec. V explores the relation of these predictions to tilting by the shear. Conclusions are offered in Sec. VI. Sensitivity analyses of the detection scheme are collected in an appendix.

## II. THE THEORETICAL MODEL

The streamwise, wall-normal, and spanwise coordinates are  $x, y, z$ , the corresponding velocity components are  $u, v, w$ , and we drop from the equations of motion the fluid density  $\rho = 1$ . We use as primary data sets simulations of turbulent channels whose half-width is  $h$ . Quantities normalized with the kinematic viscosity  $\nu$  and with the friction velocity  $u_\tau$  are denoted by a “+” superscript, and our primary Reynolds number is  $h^+$ . Although bursting is not an exclusively linear process, we have seen in the Introduction that it involves the direct interaction of the perturbations with the mean shear, and we will simplify our analysis by comparing the flow with solutions of the linearized perturbation equations for  $v$ .

For a parallel shear flow whose mean velocity profile is  $U(y)$ , small perturbations of the wall-normal velocity satisfy the autonomous linearized Navier–Stokes (Orr–Sommerfeld) equation,<sup>6,25</sup>

$$(\partial_t + U\partial_x)\nabla^2 v = U''\partial_x v + \nabla^2(\nu_T\nabla^2 v) - 2\nu_T''(\partial_{xx} + \partial_{zz})v, \quad (1)$$

where primes denote derivatives with respect to  $y$ . An eddy viscosity  $\nu_T$  that includes the molecular viscosity has been added to the right-hand side of this equation, and will be the only nonlinear effect considered in our analysis. If we define the shear  $S = U'$ , we will test the effect of dissipation by comparing results using the viscosity required to maintain the observed mean velocity profile,  $\nu_T^+ = (1 - y/h)/S^+$ , with those in which the viscosity is turned off. The inviscid problem makes sense for  $v$ , because the boundary condition at the walls,  $v = 0$ , is independent of viscosity.

Even when  $\nu_T$  is included, its effect on the large scales is weak. The usual rule of thumb in shear flows is that the equivalent Reynolds number based on the eddy viscosity is relatively large,  $O(20 - 30)$ .<sup>26</sup> Equivalently, the time scale of the shear,  $S^{-1}$ , is typically shorter than the turbulent dissipation time,  $q^2/\varepsilon$ , where  $q$  is the total velocity fluctuation magnitude and  $\varepsilon$  is the energy dissipation rate. The Corrsin shear parameter  $S^* = Sq^2/\varepsilon$  measures the ratio of those two scales,<sup>27</sup> and is of the order of  $S^* \approx 10$  in most equilibrium shear flows.<sup>19</sup> In channels, this is true across the layer  $\Lambda \approx (30\nu/u_\tau < y < 0.7h)$ .<sup>7</sup> We will use this range as our definition of the shear-dominated “logarithmic” layer, and compute most “bulk” values over it. If we take the shear and dissipative time scales as measures of the relative magnitude of the inviscid and dissipative terms in (1), the latter are small with respect to the former,  $O(1/S^*)$ . The decay time associated with the molecular viscosity,  $O(y^2/\nu)$ , is even longer than that associated with  $\nu_T$ . If we define a viscous shear parameter in the same spirit as above,  $S_\nu = Sy^2/\nu$ , and assume  $\varepsilon \approx u_\tau^3/y$  and  $q \approx u_\tau$ , it follows that  $S_\nu \approx S^*y^+$ , and that the effect of the molecular viscosity is negligible except in the immediate vicinity of the wall. Note that the range of wall distances used here is not the usual logarithmic layer. Our estimates only hold for the structures of size  $O(y)$  that are the subject of this paper. They do not necessarily apply to quantities whose evolution is slower than that of individual structures, and in particular to the mean profiles.<sup>28,29</sup> On the other hand, the criterion based on the dominance of the shear, which is a time rather than a length scale, is close enough to the usual definition of the logarithmic layer<sup>26</sup> to justify our borrowing of the name. From the point of view of the large scales above the buffer layer, the flow can be considered inviscid to a first approximation, both from the molecular and from the “eddy” point of view. As a sanity check, some of the calculations in the paper are repeated in the Appendix for a more conventional definition of the logarithmic layer,  $\Lambda_s = (150\nu/u_\tau < y < 0.4h)$ .

The first term in the right-hand side of (1) is responsible for the Kelvin–Helmholtz instability, and is not relevant to flows without inflection points. It was shown in Ref. 7 that the solutions to (1) take the form of bursts that are similar in turbulent channels and in homogeneous shear turbulence. Since  $U''$  is identically zero for the homogeneous case, this strongly suggests that only the differential advection in the left-hand-side of (1) is relevant to bursting.

In fact, the best known particular case of (1) is the homogeneous shear  $U = Sy$ , for which analytic solutions are known (e.g., see Ref. 7). If  $\nu_T$  is constant and we consider a pure Fourier mode of wavenumber  $k$ , the elementary solutions to (1) take the form

$$v = \frac{1}{1 + S^2 t^2} e^{-St(1+S^2 t^2/3)/Re+ik(x-Syt)}, \quad (2)$$

where  $Re = S/k^2\nu_T$ . They can be interpreted as plane waves whose wavefronts are tilted at an angle  $\psi = \text{atan}(St)$  with respect to  $y$ . In the inviscid case,  $\nu_T = 0$ , Eq. (2) becomes

$$v = \cos^2(\psi) e^{ik(x-y \tan \psi)}. \quad (3)$$

Form (2) of the solution only applies to a uniform shear, but it was shown in Ref. 7 that (3) is relatively independent of the mean profile if the amplitudes and tilting angles are properly defined. Equations (2) and (3) represent a pulse of  $v$  that grows and decays while the wavefronts are tilted forward by the shear, from  $\psi = -\pi/2$  at  $t \rightarrow -\infty$  to  $\pi/2$  at  $t \rightarrow \infty$ . In both limits,  $v \rightarrow 0$ , and the intensity of the wave is maximum at  $\psi \approx 0$ . This is the behavior that we will try to identify in the turbulent simulations.

Note that this description of the flow is different from the more classical decomposition in terms of wavetrains of fixed amplitude and phase speed, and is a more natural representation of intermittent situations dominated by transient growth. For example, the temporal evolution of the inviscid limit of (2) can be Fourier transformed in terms of wavetrains of phase speed  $c$  as

$$v = \frac{e^{ik(x-Syt)}}{1+S^2t^2} = \frac{k}{2} \int_{-\infty}^{\infty} e^{-k|Sy-c|+ik(x-Syt)} dc. \quad (4)$$

Each of the elementary wavetrains in this expansion has a corner discontinuity at the ‘‘critical layer’’  $c = Sy$ , but it is clear from the derivation that those layers and those discontinuities are artifacts of the Fourier transform, and that the solution in physical space has no singularities.

In simulations in a periodic box, the Fourier transform is substituted by a series. We define Fourier modes labeled by their two wall-parallel wave indexes  $(m, n)$ , as in

$$v = \sum \widehat{v}_{mn}(y) \exp 2\pi i(m x/L_x + n z/L_z). \quad (5)$$

Individual modes are attractive for the analysis of linearized approximations, but they do not represent individual flow structures. The structures of  $v$  are roughly isotropic in the three coordinate directions,<sup>19</sup> while Fourier modes are periodic and of wall-parallel infinite extent. For example, if we represent an isolated structure of size  $\lambda$  by a single Fourier mode of that wavelength, we obtain a set of weaker copies of the structure regularly distributed over the simulation box. The linear behavior of the two representations may be the same, but their nonlinear interactions with the rest of the flow are completely different. Localized structures can only be represented by wave packets with a spread of wavenumbers, which complicate their evolution equation. The only exceptions are the first few Fourier modes in a minimal box, which is defined as containing most of the energy of a ‘‘functional’’ turbulent structure in the lowest Fourier modes. In that case, the Fourier periodicity is provided by the simulation box itself.

We therefore restrict ourselves to the analysis of the first few Fourier modes,  $m = 0, 1, 2$  and  $n = 0, 1$ , each of which is taken to represent an individual structure of a different type within some range of wall distances. Mode  $\widehat{v}_{01}$  is an infinitely long streamwise streak (or roller),  $\widehat{v}_{10}$  is a two-dimensional wave in the  $(x, y)$  plane, and  $\widehat{v}_{11}$  and  $\widehat{v}_{21}$  are low-order oblique modes, each of which includes the two independent coefficients of  $n = \pm 1$ . The mean wall-normal velocity  $\widehat{v}_{00}$  vanishes identically from continuity. For the reasons mentioned in the Introduction, the study of higher-order modes, potentially representing several structures, is not attempted in this first approach to the identification problem.

Note that descriptions in terms of transient events or stationary wavetrains need not be exclusive. It is probably true that different phenomena are best represented in different ways. Uniform wavetrains and their associated critical layers have been shown to be useful in describing some aspects of turbulence,<sup>30</sup> and nonlinear analogs with non-planar critical layers have been developed for exact steady-wave solutions of the Navier–Stokes equations.<sup>31,32</sup> Intermediate wavelengths in channels are known to advect with velocities that are very close to the local mean-stream velocity, and are therefore ‘‘critical’’ everywhere,<sup>33,34</sup> as in (4). We will see below that the same is true for the low Fourier modes considered here. It also holds for wall-attached individual structures in the logarithmic layer. It was shown in Ref. 24 that individually segmented structures of intense tangential Reynolds stress are not dispersive, and that the group velocity of their wall-parallel sections is very close to the advection (phase) velocity of the individual wavenumbers. Although the structures

of  $v$  were not specifically addressed in that investigation, the Reynolds stress is carried by the vertical velocity, and it is likely that the bursts of  $v$  behave similarly. Such structures are deformed continuously by the shear and are likely to be described best by transient models. On the other hand, structures that are either very large ( $L_x \gtrsim 2h, L_z \gtrsim h/2$ ),<sup>34</sup> or restricted to the buffer layer,<sup>33</sup> have advection velocities that are independent of  $y$  over some range of wall distances. Those structures are probably best described as wavetrains with critical layers. In this paper, we will be primarily concerned with structures of the first kind.

### III. NUMERICAL DATA SETS

We use two simulations of spatially periodic channels at moderate Reynolds numbers with wall-parallel periods  $L_x = \pi h/2$  and  $L_z = \pi h/4$ , and  $h^+ = 950$  (C950)<sup>7</sup> and  $h^+ = 1850$  (C1850).<sup>12</sup> Both have been described before. To improve statistics, they have been extended in time to  $tu_\tau/h = 139$  for C950, and to  $tu_\tau/h = 69$  for C1850, and re-sampled to a common time interval between frames,  $\Delta tu_\tau/h \approx 0.025$ . Since we will see below that the typical bursting time is  $tu_\tau/h \approx 0.5$ , each simulation contains a few hundred bursts per wall, and about 20 samples per burst.

Such simulations are minimal within the band of wall distances  $y/h \approx 0.2$ – $0.5$ , in the sense that a non-negligible fraction of the energy of  $v$  is contained in the first few largest wall-parallel Fourier modes.<sup>10,12</sup> Closer to the wall, the flow contains a wider range of turbulent scales and cannot be considered minimal. Farther from it, the simulations are not directly comparable to canonical turbulence, because some of the largest scales are missing.

Even in a minimal box, the four modes considered here contain only a fraction of the total  $v^2$ . Their intensity profiles are given in Fig. 1(a). The total  $v^2$  is given by the open symbols, and

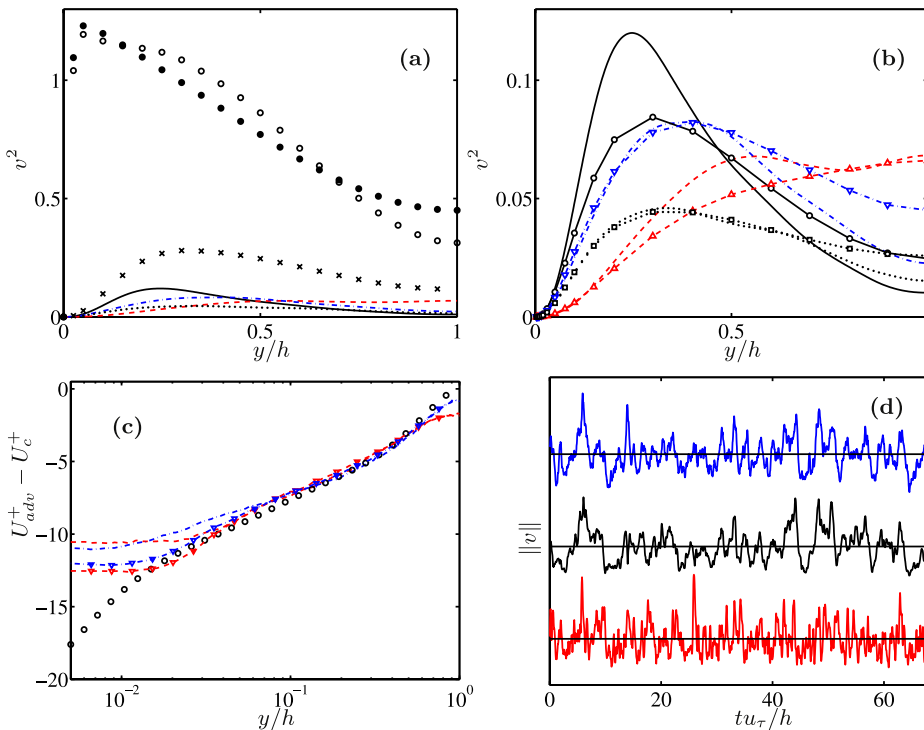


FIG. 1. (a) Intensity of the four Fourier modes considered in the minimal channel C1850. —,  $|\widehat{v}_{01}|^2$ ; ---,  $|\widehat{v}_{10}|^2$ ; - · - · -,  $|\widehat{v}_{11}|^2$ ; - · - · - · -,  $|\widehat{v}_{21}|^2$ ; ×, sum of the four modes; ○,  $|v^2|$  for C1850; ●,  $|v^2|$  for a channel at  $h^+ = 2003$ , simulated in a larger box.<sup>35</sup> (b) The lines without symbols are as in (a), compared to the corresponding intensities of the modes in the large-box channel (with symbols). (c) Advection velocities in defect form for: ---,  $\widehat{v}_{10}$ ; - · - · -,  $\widehat{v}_{11}$ . Lines with symbols are C950, those without are C1850. Open circles are the mean velocity profile for C1850. (d) Temporal evolution of the intensities integrated over the logarithmic layer. The upper trace is the full wall-normal velocity; the middle one is the streak  $\widehat{v}_{01}$ , and the lowest one is  $\widehat{v}_{10}$ . C1850.

a simulation in a larger box and similar Reynolds number is given by the closed ones. The figure shows that the combined contribution of our four modes is at most 25%–30% of the total, attained around  $y/h = 0.25 - 0.8$ . Figure 1(b) is an enlargement of their intensity profiles, compared with the corresponding profiles for the channel in the larger box. It is seen that the accuracy of the individual Fourier modes in the minimal simulation is comparable to that of the overall intensity. Note that there is no unique way of comparing Fourier modes between boxes of different sizes, because there are several possible associations of blocks of the higher-resolution spectrum of the larger box with individual modes of the smaller one. Figure 1(b) is drawn by comparing individual modes of the smaller box with the energy in a uniform tiling of the wavenumber plane of the larger one, properly chosen to take into account the corresponding spectral resolutions. Other blocking strategies give qualitatively similar results.

Fig. 1(c) shows the advection velocities of  $\widehat{v}_{10}$  and  $\widehat{v}_{11}$ , defined as in Ref. 34. They agree well with the results in that reference. They follow the mean velocity profile over most of  $\Lambda$ , implying that the modes are continuously tilted by the shear. Comparing Figs. 1(b) and 1(c), the advection velocity changes by approximately  $5u_\tau$  over the wall-normal extent of the modes in question. The top of each mode is therefore shifted with respect to its bottom by a full wavelength ( $L_x = \pi/2$ ) in a fraction of a turnover,  $u_\tau \Delta t/h \approx \pi/10$ , suggesting that the bursting time should be of that order.

Note that the linearized interaction of  $v$  with the mean shear involves only terms with streamwise derivatives. Modes with  $m = 0$  evolve only under the effect of viscosity, and  $\partial_t \widehat{v}_{0n} = 0$  in the linear inviscid limit. It is impossible to define either a streamwise advection velocity or tilting for these modes.

Figure 1(d) displays the evolution of the  $L_2$  velocity seminorm,

$$\|\widehat{v}_{mn}\|^2 = h^{-1} \int_{\Lambda} |\widehat{v}_{mn}|^2 dy. \quad (6)$$

It shows that the individual Fourier modes also burst. Statistically, they are slightly more intermittent than the total velocity. The fourth- and sixth-order flatness of the time evolution of the amplitude of the modes with  $m \neq 0$  are  $F_4 \approx 4$  and  $F_6 \approx 40 - 50$ , while those of the overall  $\|v\|$  are  $F_4 \approx 3.5$  and  $F_6 \approx 20$ . The corresponding Gaussian values are  $F_4 = 3$  and  $F_6 = 15$ . The more Gaussian behavior of the total energy is in agreement with the central-limit theorem, that predicts Gaussian distributions for sums of uncorrelated variables, but it is interesting that the moments of the roller mode  $\widehat{v}_{01}$  are almost exactly Gaussian. This is the only one of our modes that does not interact with the shear, suggesting again that bursting is shear-controlled. The integrated amplitudes of the individual modes are only weakly correlated with each other, with correlation coefficients between the  $\|\widehat{v}_{mn}\|$  of the order of  $C_{\|v\| \|v\|} = 0.1$ . The same is true for the intensities in the two halves of the channel. The correlation between the intensity of individual modes and that of the total velocity is somewhat higher, with correlation coefficients of the order of 0.5 for all the modes considered here.

It is clear from Fig. 1(d) that different modes burst with different periods. The “roller” mode in the middle trace is the slowest, and follows the behavior of the full velocity (top trace) rather closely. The bottom trace,  $\|\widehat{v}_{10}\|$ , has a faster cycle of its own. The same is true for the oblique mode  $\|\widehat{v}_{11}\|$ , and for  $\|\widehat{v}_{21}\|$  (not shown). We saw above that only modes with  $m \neq 0$  interact “linearly” with the shear, and it is not surprising that they behave differently from those with  $m = 0$ . It has to be stressed that different Fourier modes may represent different structures, as shown, for example, by their different profiles in Fig. 1(a). There is nothing against the coexistence of different linear structures in the same simulation, but even nonlinear ones can coexist. The simplest way is for different structures to be active at different times, but other arrangements are possible in multiscale turbulence. The situation is similar to the behavior of the different velocity components that, although presumably related to each other by the equations of motion, have different spectral content and spatial correlations.<sup>35,36</sup> In principle, each of the Fourier modes considered here is the leading term of the spectral expansion of a nonlinear structure. Even linearly, each of them is the sum of several  $y$ -eigenfunctions, each of which could be interpreted as the leading term of a different structure. We will see later that, although there are times in which the evolution of each mode is well represented

by a single vertical eigenfunction that behaves as an independent linearized entity, the situation in other moments is more complicated and nonlinear.

**IV. THE PERFORMANCE OF LINEARIZED PREDICTIONS**

The bursting time, defined as the average width of individual bursts, can be measured in minimal boxes by the width of the temporal autocorrelation functions of the box integrals of the relevant quantities,

$$C(t) = \frac{\langle \|v\|(\tau) \|v\|(\tau + t) \rangle}{\langle \|v\|^2 \rangle^{1/2}}, \tag{7}$$

where  $\langle \rangle$  is the average over  $\tau$  and over ensembles (both walls). The correlations are given for the different  $\|v_{mn}\|$  in Fig. 2(a). When the integration of the seminorm is done over a narrow band of wall distances, the correlation time scales with the local mean shear.<sup>7</sup> Here, because we are interested in global properties affecting the whole channel, Fig. 2(a) is computed for quantities integrated over the logarithmic layer  $\Lambda$ , as in (6). The relevant time scale then becomes  $h/u_\tau$ , but the bursting time, defined as the width of the autocorrelation at  $C(t) = 0.5$ , depends on the mode considered and cannot be easily scaled with local quantities. The bursting time is  $u_\tau T_b/h \approx 0.4$  for  $\|\widehat{v}_{10}\|$  and  $\|\widehat{v}_{11}\|$ , which is of the order estimated above from the advection velocities. The correlation time for  $\|\widehat{v}_{21}\|$ , whose streamwise wavelength is only half that of  $\|\widehat{v}_{11}\|$ , is twice shorter,  $u_\tau T_b/h \approx 0.2$ . For  $\|\widehat{v}_{01}\|$ , which does not interact directly with the shear, the bursting time is  $u_\tau T_b/h \approx 1.1$ , longer than for the full velocity,  $u_\tau T_b/h \approx 0.9$ . The effect of integrating over

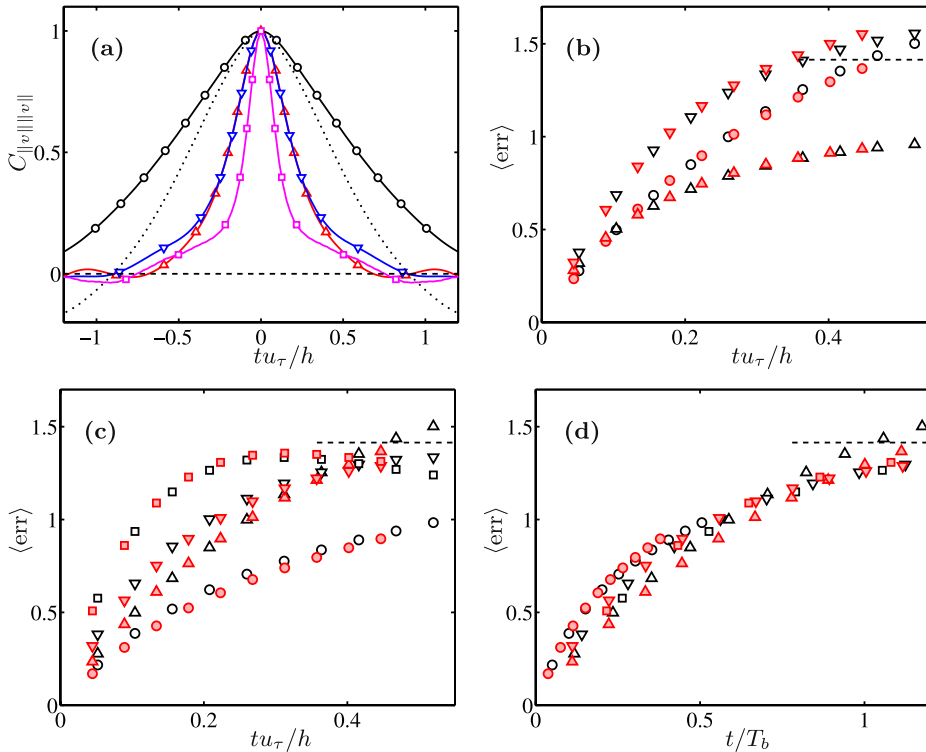


FIG. 2. (a) Temporal auto-correlation of velocity seminorm (6), integrated over  $\Lambda$ . Symbols in lines:  $\circ$ ,  $\|\widehat{v}_{10}\|$ ;  $\Delta$ ,  $\|\widehat{v}_{11}\|$ ;  $\nabla$ ,  $\|\widehat{v}_{21}\|$ ;  $\square$ ,  $\|\widehat{v}_{01}\|$ ; - - - - -,  $\|v\|$ . C1850. (b) Root-mean-squared error for the predictions of  $\widehat{v}_{10}$ , as a function of the predicted time interval, defined as in (8).  $\nabla$ , using pure advection with the mean velocity profile as a predictor;  $\circ$ , using the inviscid linearized Navier–Stokes approximation (1);  $\Delta$ , Eq. (1) with eddy viscosity. (c) As in (b) for different Fourier modes and inviscid linearized Navier–Stokes. Symbols for the different Fourier modes, as in (a). (d) As in (c), with time scaled with the bursting width defined at  $C = 0.5$  in (a). The horizontal dashed line in (b)–(d) is the relative error,  $\sqrt{2}$ , between two uncorrelated signals of the same intensity. Open symbols, C950; closed, C1850.



a narrower vertical range is slight, as shown in Fig. 6(a) of the Appendix. The same is true for the differences between the two Reynolds numbers. The Eulerian decorrelation time for full complex modes such as  $\widehat{v}_{10}$  is much shorter than the one for their norm, because their phase varies faster than their amplitude as the flow is carried past a given point by the local advection velocity.

A measure of the decorrelation time more closely related to our present task is the decay of the accuracy of the flow predictions made using linearized equation (1) as a model. Note that those predictions need to consider the full channel, with boundary conditions at both walls, but that the error can be defined over a narrower layer such as  $\Lambda$ . For consistency with the rest of the paper, the errors between a mode  $\widehat{v}$  and its prediction  $\widehat{v}_p$  are defined as

$$\text{err} = \|\widehat{v}_p - \widehat{v}\|/\|\widehat{v}\|. \quad (8)$$

This is an instantaneous value for individual predictions, and Fig. 2(b) shows its ensemble average,  $\langle \text{err} \rangle$ , for three predictors as a function of the prediction time. It was shown in Ref. 7 that the Eulerian acceleration in a channel is mostly contained in the linear terms of the equations, and that most of it is explained by the advection by the mean flow. Figure 2(b) shows that this is not true for the evolution of the velocity over non-infinitesimal time periods. The inverted triangles in the figure use the simple advection predictor  $\widehat{v}_p(y, t + \Delta t) = \widehat{v}(y, t) \exp[-ik_x U(y) \Delta t]$ . They behave worse than the other two predictors in the figure at all times, including very short ones. The inviscid linearized approximation represented by circles behaves well for short times, but degrades for periods of the order of the bursting time. For longer times, both inviscid predictors approach the error level between two uncorrelated signals. The triangles in the figure use Eq. (1) with eddy viscosity. They do not behave better than the inviscid model for short times, but they level off at  $\langle \text{err} \rangle \approx 1$  for longer times. Unfortunately, this does not reflect an increased long-term accuracy of the viscous approximation. The amplitude of the viscous prediction tends to zero for times longer than the bursting time, and the difference between the true velocity and its predictor tends to the value of the true velocity. The relative error then tends to unity, which is less than the relative error between two uncorrelated signals of similar magnitude. Note that the collapse of the error curves for the two Reynolds numbers in Fig. 2 supports the use of the eddy turnover  $h/u_\tau$  as a time scale.

The predictions for the four Fourier modes used in this paper are compared in Figs. 2(c) and 2(d). In general, the prediction error degrades as the modes become more complex, with the oblique mode  $\widehat{v}_{21}$  always predicted worst. However, the relative behavior of the four modes can be largely explained by their different bursting times. While the four modes behave differently when expressed in terms of a common time scale, as in Fig. 2(c), their errors collapse much better when the prediction interval is scaled with the respective bursting times, as in Fig. 2(d). This is especially true for the three modes that interact with the shear, for whom linear predictions work reasonably well for periods of the order of half of the bursting time. The dependence on the choice of  $\Lambda$  is tested in Fig. 6(b) in the Appendix. It is relatively minor.

The good scaling of the linear prediction error with  $T_b$  is interesting in view of the shape of the correlations in Fig. 2(a). Specially for the higher modes, they have two components: a highly correlated narrow core, and a wider skirt that becomes more prominent as the modes become more complex. Our definition of the correlation time measures the width of the inner core, and it is tempting to identify it with linear bursting. The skirt, whose width is closer to that of the full velocity, would be associated with slower nonlinear interactions among several modes.

## V. TILTING

Further insight can be obtained by comparing the detailed temporal evolution of the linearized and full equations. The essence of an Orr burst is that the structures are tilted downstream by the differential advection of the shear. As the wavefronts become roughly normal to the wall, the vertical length scale increases, and continuity requires that  $|\widehat{v}|$  increases to conserve  $\partial_y \widehat{v}$ . As the wavefronts are tilted past that point,  $|\widehat{v}|$  decreases again. If we write  $\widehat{v} = |\widehat{v}| \exp[i(k_x x + \phi)]$ , the derivative  $k_y = \partial_y \phi$  is a vertical wavenumber, and  $\psi = -\text{atan}(k_y/k_x)$  is a front inclination angle. While the wavefronts in a uniform shear are planar, the tilt and the amplitude in a channel are functions of  $y$ , and it was shown in Ref. 7 that the equivalent quantities have to be integrated over

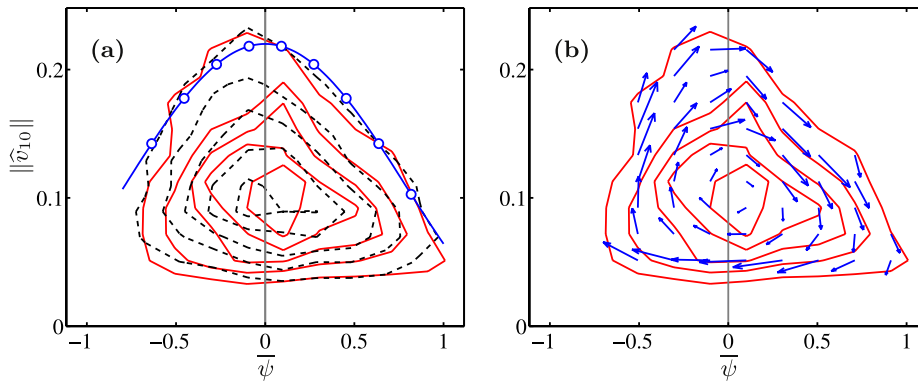


FIG. 3. (a) Two-dimensional joint probability distribution function of the mean inclination and amplitude of  $\widehat{v}_{10}$  in the direct simulations. —, C1850; ---, C950; —○—,  $\|\widehat{v}_{10}\| = \cos^2(\bar{\psi})$ , is the linear inviscid result for a uniform shear, as in (3). The contours contain 0.1(0.2)0.9 of the total number of samples. (b) As in (a), for the C1850 channel. The arrows indicate the mean conditional evolution of the two quantities.

the intense part of the wave. Here, we define the mean amplitude as seminorm (6), and the mean inclination angle as the weighted average  $\bar{\psi} \|\widehat{v}\|^2 = h^{-1} \int_{\Lambda} |\widehat{v}|^2 \psi \, dy$ . It is with those definitions that relation (3) between tilt and amplitude is approximately universal.

Equation (3) is plotted as a solid line with circles in Fig. 3(a), and has two important properties. The first is that the amplitude of  $v$  is maximum at  $\bar{\psi} \approx 0$  and symmetric with respect to  $\bar{\psi}$ . The second is that the angle is traversed from left to right. The corresponding trajectories in the minimal channel are too irregular to be analyzed individually, but Fig. 3(a) contains the joint probability density function (p.d.f.) of the instantaneous mean tilt and amplitude in the minimal channel. It satisfies the first of the two properties mentioned above. It is approximately symmetric in  $\bar{\psi}$ , and maximum at the center. The intensities are low near  $\bar{\psi} = \pm\pi/2$ . Although not being considered in this paper, neither  $u$  nor  $w$  share this property: their p.d.f.s are clearly tilted towards positive angles. The p.d.f.s of the two Reynolds numbers agree within the statistical uncertainty, underscoring the inviscid nature of the behavior. The p.d.f. for C1850 is repeated in Fig. 3(b), where the arrows represent the temporal evolution,  $(\partial_t \|\widehat{v}\|, \partial_t \bar{\psi})$ , conditioned to each neighborhood of the  $(\|\widehat{v}\|, \bar{\psi})$  plane. The upper part of the p.d.f.s of the minimal flows agrees well with the linearized prediction, and is traversed by the flow in the right direction. This rightwards flow of the angles of the intense structures is not a statistical artifact. It is shown in Fig. 7(b) of the Appendix that, if the order of the time series of the angles is randomized before compiling the temporal evolution, the clockwise flow of the arrows in Fig. 3(b) is destroyed. The Appendix also tests that the general features of the p.d.f. in Fig. 3 are robust to the choice of  $\Lambda$ .

The bias of the p.d.f. towards negative angles, and its longer tail towards the right-hand side of the plot are statistically robust in the sense that they survive after randomly discarding half of the data points in each experiment. They are also found in both Reynolds numbers, and in an older experiment at  $h^+ = 950$  that is not used in this paper because of its coarser temporal resolution. Although the bias is relatively small, it is consistent with the effect of dissipation. Any eddy viscosity tends to damp wavefronts that are too tightly packed because they are very tilted in either direction. Towards the end of the burst, the effect is not important, because it just reinforces the natural inviscid decay. Its effect on the central part of the burst is also moderate, because the vertical scale is large. On the other hand, very tilted waves at the beginning of the burst are damped before they have a chance to grow, setting a limit to the initial negative tilt of the bursts that survive. This effect can be easily checked in analytic formula (2) for the uniform-shear case, where viscosity also moves the maximum intensity to slightly negative angles, as in Fig. 3. However, the effect is too dependent on the Reynolds number and on the eddy viscosity model to allow quantitative comparisons.

The right-to-left evolution in the lower edge of Fig. 3(b) is contrary to the prediction of linear models. It needs to be explained, although it should be noted that some kind of return path is required for the statistical survival of the flow. Two short segments of the temporal evolution of the

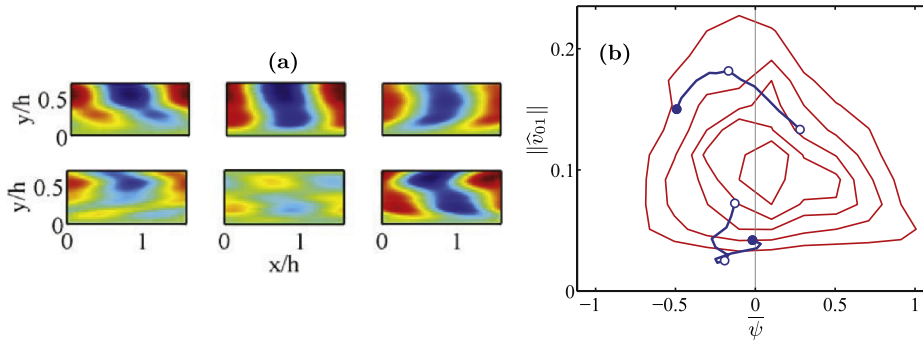


FIG. 4. (a) Two evolution histories of  $v_{10}$ , corresponding to the trajectories marked in the p.d.f. in (b), both of which start with a closed circle. The time increment between frames (circles in (b)) is  $u_\tau \Delta t / h = 0.135$ , from left to right. The upper row corresponds to the upper trace in (b), and vice versa. Only  $y < 0.7h$  is represented. C1850. (b) Tilt–amplitude joint p.d.f. for  $\hat{v}_{10}$ , as in Fig. 3. The two trajectories correspond to the snapshots in (a).

flow field of  $v_{01}$  are shown in Fig. 4(a). The top row displays three frames along a trajectory near the upper edge of the joint p.d.f. (upper trace in Fig. 4(b)). It represents a burst, and clearly shows how the wavefronts are progressively tilted forward by the shear. The trace in Fig. 4(b), in which the three symbols correspond to the three frames, shows how the wave is strengthened as it becomes vertical, and then weakens as in the Orr burst.

The lower row in Fig. 4(a) corresponds to the irregular trajectory near the lower edge of Fig. 4(b), and suggests the reason why only the upper part of Fig. 3(b) follows the linear predictions. The mean inclination angle and amplitude used here are integrated over the logarithmic layer in one half of the channel, because it is otherwise difficult to define a unique angle. Figure 4 shows that some attempts to define an inclination angle are bound to fail because they involve parts of the channel in which the wavefronts are not well defined. In fact, simple solutions such as (2) depend on simple initial conditions, which in the case of (2) are pure Fourier modes whose vertical wavenumber is a function of time. In the channel, each wall-parallel wavenumber has an associated eigensolution in  $y$  whose form also changes with time. It is very tightly packed at the beginning of the burst, unwinds as  $\bar{\psi} \approx 0$ , and winds up again after that. Because of the variable vertical structure, the linear superposition of several bursts with different time origins results in more complicated vertical structures. The lower row of Fig. 4(a) suggests that the flow contains such multiple structures at the times of low fluctuation intensity, and cannot be easily described in terms of a single tilt or amplitude.

This is quantified in Fig. 5(a). The inclination angle  $\psi$  is a function of  $y$ , and the flow can only be expected to be well described by a single inclination angle if the standard deviation of  $\psi$  with respect to its mean is reasonably small. This standard deviation is computed, as before, using the squared perturbation amplitude as a weight. It is shown in Fig. 5(a) as a map over the angle–amplitude parameter space of Fig. 3. The standard deviation is only small in the upper half of the p.d.f., which corresponds to wavefronts such as those in the upper row of Fig. 4(a). This well-represented region spans 30%–50% of the time in our sample. The lower row of Fig. 4(a) corresponds to the lower part of the  $(\|\hat{v}\|, \bar{\psi})$  map, where the standard deviations of  $\psi$  are large, and the attempt to describe the flow in terms of coherent wavefronts fails.

More interesting than whether the flow can be qualitatively described by models inspired by linearized approximations is whether the linearized equations can be used to predict it. We saw in Fig. 2 that the average error of such predictions remains reasonable over times of the order of a fraction of the bursting period, but it was unclear at the time whether the accuracy of those predictions was in any way connected to bursting. This is tested in Fig. 5(b), which presents the distribution over the tilt–amplitude plane of the relative error of the predictions of  $\hat{v}_{10}$ , using the inviscid version of Eq. (1). For the particular prediction time chosen,  $u_\tau \Delta t / h = 0.135$ , the average relative error is approximately 0.5, but it is clear from Fig. 5(b) that strong events are better predicted, while weaker ones are predicted worse. Comparison with Fig. 5(a) reveals that the poorly predicted cases correspond to flows in which the wave fronts are not well defined, even if linearized

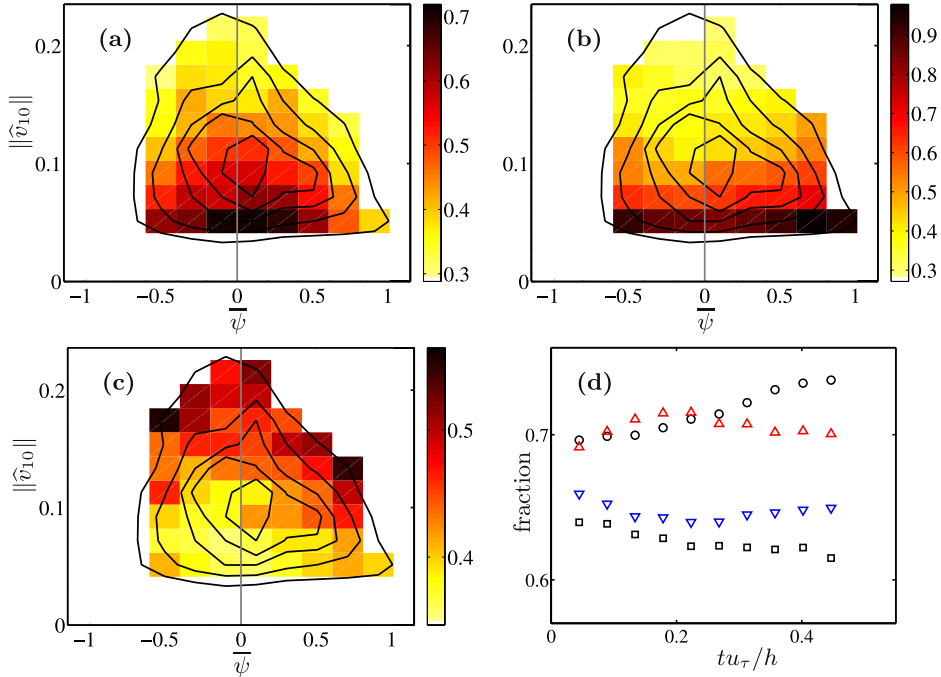


FIG. 5. (a) Colors represent the standard deviation of the wavefront inclination angle with respect to its mean, in the same parameter space as Fig. 3. (b) Same as (a), but colours represent the relative error of the inviscid linearized prediction from  $\widehat{v}_{10}(t - \Delta t)$  to  $\widehat{v}_{10}(t)$ , with  $u_\tau \Delta t/h = 0.135$ . C1850. (c) As in (b), but colors represent the absolute error of the inviscid linearized prediction,  $\langle \|\widehat{v}_p - \widehat{v}\| \rangle / \langle \|\widehat{v}\| \rangle$ . (d) Fraction of time in which the instantaneous relative error of the inviscid linearized prediction is smaller than its mean,  $\text{err} < \langle \text{err} \rangle$ .  $\circ$ ,  $|\widehat{v}_{01}|^2$ ;  $\Delta$ ,  $|\widehat{v}_{10}|^2$ ;  $\nabla$ ,  $|\widehat{v}_{11}|^2$ ;  $\square$ ,  $|\widehat{v}_{21}|^2$ .

equation (1) does not explicitly depend on a simple flow structure. The prediction time interval used to draw Fig. 5(b) is the one between frames in Fig. 4(a), or between symbols in Fig. 4(b). It is a sizable fraction of the bursting time. The average change of the inclination angles over that period is  $\Delta\psi \approx 0.45$ , close to one third of the total range of angles in the figure. Results similar to the ones discussed here for  $\widehat{v}_{10}$  are obtained for the oblique modes  $\widehat{v}_{11}$  and  $\widehat{v}_{21}$ . Because a tilt angle cannot be defined for mode  $\widehat{v}_{01}$ , an analysis such as the one in Fig. 5(b) cannot be made for that mode, but it is also true that its relative prediction error decreases with increasing amplitude.

A somewhat different view of the prediction error is Fig. 5(c), in which the colors represent the *absolute* error  $\langle \|\widehat{v}_p - \widehat{v}\| \rangle / \langle \|\widehat{v}\| \rangle$ . Its range of values is much narrower than for the relative error in Fig. 5(b),  $\langle \|\widehat{v}_p - \widehat{v}\| \rangle / \langle \|\widehat{v}\| \rangle$ , and is actually slightly higher for the more intense perturbations than for the weaker ones. The simplest interpretation of these two figures is that there is an “irreducible” nonlinear component of the flow evolution that cannot be predicted linearly. When a linear burst is not active, as in the lower part of Fig. 5(b), it dominates the flow and the prediction is poor. When bursting is active, as in the upper part of Fig. 5(b), the predictable linear component represents most of the perturbation and the relative error is small. A consequence of this behavior is that the shape of the p.d.f. of the relative error is mostly controlled by the intermittency of its denominator,  $\|\widehat{v}\|$ . It is fairly independent of the prediction time and, up to a point, of the particular mode involved. This is seen in Fig. 5(d), which shows the fraction of time in which the relative error of a given prediction is below its mean,  $\text{err} < \langle \text{err} \rangle$ . It is relatively constant, at 65%–70% for the four modes considered, and remains so for all the prediction times, including those in which Fig. 2(c) shows that the prediction is essentially uncorrelated to the real flow.

## VI. CONCLUSIONS

We have shown that some large-scale modes of the wall-normal velocity in a fully nonlinear turbulent minimal channel can be well described as transient Orr bursts, at least part of the time.

This leads to their linearized predictability over times which, in our channels, are  $O(0.15 h/u_\tau)$ . This corresponds to advection lengths of a few boundary-layer thickness. The degradation of predictability over longer times has been shown to be a consequence of the appearance of more complex flow fields that cannot be described by simple wall-normal eigenfunctions, and which cannot be described linearly. On the other hand, nonlinearity is overwhelmed by the linear bursting process while the latter is active. Bursts appear to be essentially inviscid, and the addition of an eddy viscosity does not improve the predictions appreciably. It is tempting in this respect to recall the criterion for the relevance of nonlinear effects in forced shear layers,<sup>37</sup> which is that nonlinearity only matters when the growth of the layer pushes the prevailing wavenumber outside the instability range of the linear Kelvin–Helmholtz mechanism. The argument in that case is a comparison of time scales similar to the one used here to justify linearity. As long as the shear time is the fastest one, nonlinearity is irrelevant. Only when the flow decouples from the shear has nonlinearity time to act.

Prediction is probably one of the more practical consequences of conceptual understanding, even if the two do not always go together. From the above discussion, it is clear that they do in this case. The strong events that can be described as shear-controlled Orr bursts fill about 65–70% of the total flow history in the logarithmic layer, in the sense that the error of a linear prediction is less than the average error for a given time interval. At those moments, the flow can be predicted over relatively long times. The weaker events that cannot be described in this way are also predicted worse. It is remarkable that any linearized model is able to describe the flow reasonably well over times of the order of a substantial fraction of the bursting time, and it is striking and contrary to common intuition that the strongest events are those best described by linearized models. However, it should be emphasized that the conclusions of this paper refer to the dynamics of a few Fourier modes in minimal channels, chosen as simplified representations of single coherent structures for which identification methods could be developed. It is clear from Fig. 2(c) that higher modes are only linearly predicted for short times. That is specially clear for  $\widehat{v}_{21}$ . There is probably little hope that the full flow field can be predicted linearly for any amount of time relevant to the larger scales. The small scales are nonlinear over those times.

These conclusions remain to be extended to larger simulations in which structures are localized both in space and in time.<sup>15,20,24</sup> We have argued that the representation in terms of transient events is more natural than expansions in term of permanent wavetrains for temporally intermittent flow structures. The spatial Fourier analysis used here might be as unnatural for spatially intermittent cases as the temporal Fourier analysis has proved to be in the present one.

## ACKNOWLEDGMENTS

This work was supported by the European Research Council Multiflow Grant No. ERC-2010.AdG-20100224. I am grateful to M. Pérez-Encinar for recomputing case C950 to the required higher sampling rate.

## APPENDIX: CONSISTENCY CHECKS

This appendix collects consistency and independence checks for our numerical detection algorithms. Figure 6(a) tests the dependence of the correlation width of the different Fourier modes on the domain over which identifications are performed and errors integrated. This domain is loosely referred in the paper as the logarithmic layer, using the criterion that it is the region over which the large scales are dominated by the shear.<sup>7</sup> But, because this is only loosely connected with the conventional definition of logarithmic layer, some of the calculations are repeated here for the more restricted integration interval,  $\Lambda_s = (150\nu/u_\tau < y < 0.4h)$ . The bursting widths measured over the narrower range of wall distances in Fig. 6(a) are slightly shorter than over the wider one, but the difference is small.

Figure 6(b) displays the effect of the narrower integration domain on the errors of the linear predictions, and should be compared with Figure 2(d). Again, the results do not change qualitatively. There is a slight deterioration of the prediction accuracy for the narrower range, which is

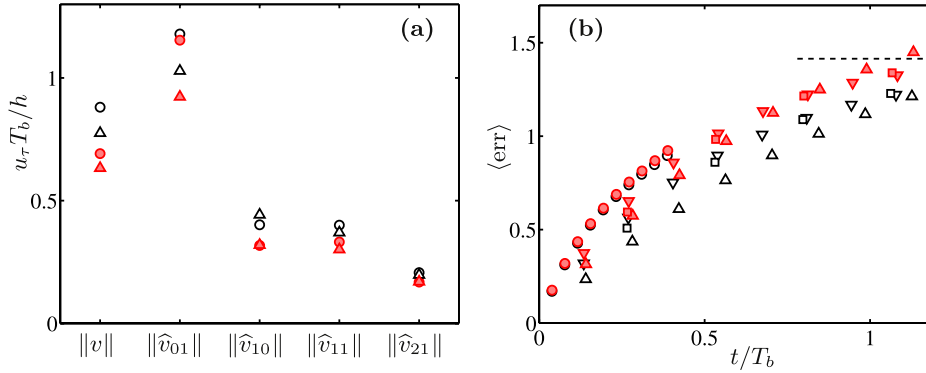


FIG. 6. (a) Correlation widths at  $C=0.5$ .  $\circ$ , C1850;  $\triangle$ , C950. (b) As in Figure 2(d). Root-mean-squared error for the predictions of different Fourier modes using the inviscid linearized Navier–Stokes model. The time is scaled with the bursting width. Case C1850.  $\circ$ ,  $\|\hat{v}_{01}\|$ ;  $\triangle$ ,  $\|\hat{v}_{10}\|$ ;  $\nabla$ ,  $\|\hat{v}_{11}\|$ ;  $\square$ ,  $\|\hat{v}_{21}\|$ . In both panels, the open symbols are integrated over  $\Lambda = (30\nu/u_\tau < y < 0.7h)$ , as in the body of the paper; closed symbols,  $\Lambda_s = (150\nu/u_\tau < y < 0.4h)$ .

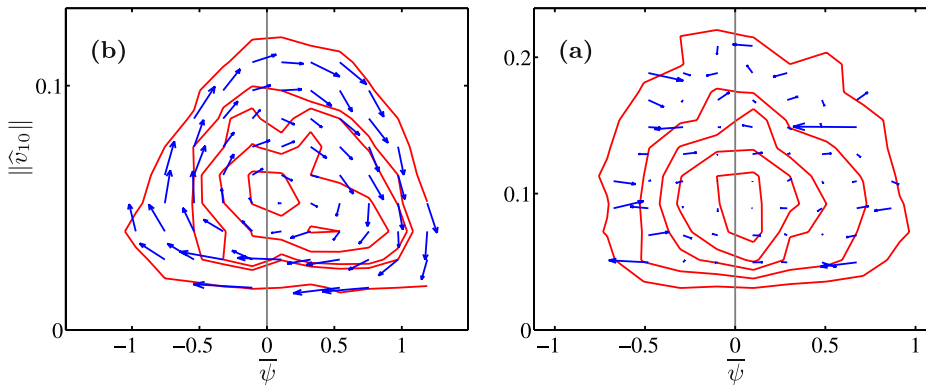


FIG. 7. (a) As in Figure 3(b). Two-dimensional joint probability distribution function of the mean inclination and amplitude of  $\hat{v}_{10}$  in case C1850. The arrows indicate the mean conditional evolution of the two quantities. Angles and amplitudes are defined over the “short” logarithmic layer  $\Lambda_s$ . (b) As in (a), but the time stamp of the angles is randomized before compiling the joint p.d.f. Scale of arrows is the same in both panels.

associated with its upper limit. It can be shown that the error is largest near the wall, where the shear is strongest, while the outer layer contributes mostly to the velocity norm used as normalization.

Figure 7 tests the robustness of the angle-amplitude correlation. Figure 7(a) is equivalent to Figure 3(b) in the body of the paper, but the average inclination angle and the amplitude are integrated over the short logarithmic layer  $\Lambda_s$ . Although there are some differences in detail between the two figures, the shape of the p.d.f. and the direction of evolution is the same. Figure 7(b) is also integrated over  $\Lambda_s$ , but the order of the time series of the angles is randomized before compiling the joint p.d.f. The marginal probabilities of the angles and amplitudes are identical to those in Fig. 7(a), since the time series involved are the same in both cases. But the joint p.d.f. is completely different, the correlation between the two quantities has disappeared, and the orderly time evolution has been destroyed.

<sup>1</sup> A. N. Kolmogorov, “The local structure of turbulence in incompressible viscous fluids at very large Reynolds numbers,” *Dokl. Akad. Nauk. SSSR* **30**, 301–305 (1941), [reprinted in *Proc. R. Soc. A* **434**, 9–13 (1991)]. Available at <http://www.jstor.org/stable/51980>.

<sup>2</sup> G. L. Brown and A. Roshko, “On the density effects and large structure in turbulent mixing layers,” *J. Fluid Mech.* **64**, 775–816 (1974).

<sup>3</sup> W. C. Reynolds and W. G. Tiederman, “Stability of turbulent channel flow, with application to Malkus’ theory,” *J. Fluid Mech.* **27**, 253–272 (1967).

<sup>4</sup> W. V. R. Malkus, “Outline of a theory of turbulent shear flow,” *J. Fluid Mech.* **1**, 521–539 (1956).

<sup>5</sup> K. M. Butler and B. F. Farrell, “Optimal perturbations and streak spacing in wall-bounded shear flow,” *Phys. Fluids A* **5**, 774–777 (1993).

- <sup>6</sup> J. C. del Álamo and J. Jiménez, “Linear energy amplification in turbulent channels,” *J. Fluid Mech.* **559**, 205–213 (2006).
- <sup>7</sup> J. Jiménez, “How linear is wall-bounded turbulence?,” *Phys. Fluids* **25**, 110814 (2013).
- <sup>8</sup> S. J. Kline, W. C. Reynolds, F. A. Schraub, and P. W. Runstadler, “Structure of turbulent boundary layers,” *J. Fluid Mech.* **30**, 741–773 (1967).
- <sup>9</sup> T. Ellingsen and E. Palm, “Stability of linear flow,” *Phys. Fluids* **18**, 487–488 (1975).
- <sup>10</sup> J. Jiménez and P. Moin, “The minimal flow unit in near-wall turbulence,” *J. Fluid Mech.* **225**, 213–240 (1991).
- <sup>11</sup> J. Jiménez, G. Kawahara, M. P. Simens, M. Nagata, and M. Shiba, “Characterization of near-wall turbulence in terms of equilibrium and ‘bursting’ solutions,” *Phys. Fluids* **17**, 015105 (2005).
- <sup>12</sup> O. Flores and J. Jiménez, “Hierarchy of minimal flow units in the logarithmic layer,” *Phys. Fluids* **22**, 071704 (2010).
- <sup>13</sup> W. Schoppa and F. Hussain, “Coherent structure generation in near-wall turbulence,” *J. Fluid Mech.* **453**, 57–108 (2002).
- <sup>14</sup> J. Jiménez and A. Pinelli, “The autonomous cycle of near wall turbulence,” *J. Fluid Mech.* **389**, 335–359 (1999).
- <sup>15</sup> J. C. del Álamo, J. Jiménez, P. Zandonade, and R. D. Moser, “Self-similar vortex clusters in the logarithmic region,” *J. Fluid Mech.* **561**, 329–358 (2006).
- <sup>16</sup> P. J. Schmid and D. S. Henningson, *Stability and Transition in Shear Flows* (Springer, 2001), pp. 55–58.
- <sup>17</sup> P. J. Schmid, “Nonmodal stability theory,” *Annu. Rev. Fluid Mech.* **39**, 129–162 (2007).
- <sup>18</sup> W. M. Orr, “The stability or instability of the steady motions of a perfect liquid, and of a viscous liquid. Part I: A perfect liquid,” *Proc. R. Ir. Acad. A* **27**, 9–68 (1907). Available at <http://www.jstor.org/stable/20490590>.
- <sup>19</sup> J. Jiménez, “Near-wall turbulence,” *Phys. Fluids* **25**, 101302 (2013).
- <sup>20</sup> A. Lozano-Durán, O. Flores, and J. Jiménez, “The three-dimensional structure of momentum transfer in turbulent channels,” *J. Fluid Mech.* **694**, 100–130 (2012).
- <sup>21</sup> A. Lozano-Durán and J. Jiménez, “Effect of the computational domain on direct simulations of turbulent channels up to  $Re_\tau = 4200$ ,” *Phys. Fluids* **26**, 011702 (2014).
- <sup>22</sup> J. M. Wallace, H. Eckelmann, and R. S. Brodkey, “The wall region in turbulent shear flow,” *J. Fluid Mech.* **54**, 39–48 (1972).
- <sup>23</sup> W. W. Willmarth and S. S. Lu, “Structure of the Reynolds stress near the wall,” *J. Fluid Mech.* **55**, 65–92 (1972).
- <sup>24</sup> A. Lozano-Durán and J. Jiménez, “Time-resolved evolution of coherent structures in turbulent channels: Characterization of eddies and cascades,” *J. Fluid Mech.* **759**, 432–471 (2014).
- <sup>25</sup> G. Pujals, M. García-Villalba, C. Cossu, and S. Depardon, “A note on optimal transient growth in turbulent channel flow,” *Phys. Fluids* **21**, 015109 (2009).
- <sup>26</sup> H. Tennekes and J. L. Lumley, *A First Course in Turbulence* (MIT Press, 1972).
- <sup>27</sup> S. Corrsin, “Local isotropy in turbulent shear flow,” NACA Res. Memo 58B11 (1958).
- <sup>28</sup> M. Wosnik, L. Castillo, and W. K. George, “A theory for turbulent pipe and channel flows,” *J. Fluid Mech.* **421**, 115–145 (2000).
- <sup>29</sup> J. Klewicki, P. Fife, T. Wei, and P. McMurtry, “A physical model of the turbulent boundary layer consonant with mean momentum balance structure,” *Philos. Trans. R. Soc., A* **365**, 823–839 (2007).
- <sup>30</sup> B. J. McKeon and A. S. Sharma, “A critical-layer framework for turbulent pipe flow,” *J. Fluid Mech.* **658**, 336–382 (2010).
- <sup>31</sup> P. Hall and S. J. Sherwin, “Streamwise vortices in shear flows: Harbingers of transition and the skeleton of coherent structures,” *J. Fluid Mech.* **661**, 178–205 (2010).
- <sup>32</sup> H. M. Blackburn, P. Hall, and S. J. Sherwin, “Lower branch equilibria in Couette flow: The emergence of canonical states for arbitrary shear flows,” *J. Fluid Mech.* **762**, R2 (2013).
- <sup>33</sup> J. Kim and F. Hussain, “Propagation velocity of perturbations in channel flow,” *Phys. Fluids A* **5**, 695–706 (1993).
- <sup>34</sup> J. C. del Álamo and J. Jiménez, “Estimation of turbulent convection velocities and corrections to Taylor’s approximation,” *J. Fluid Mech.* **640**, 5–26 (2009).
- <sup>35</sup> S. Hoyas and J. Jiménez, “Scaling of the velocity fluctuations in turbulent channels up to  $Re_\tau = 2003$ ,” *Phys. Fluids* **18**, 011702 (2006).
- <sup>36</sup> J. A. Sillero, J. Jiménez, and R. D. Moser, “Two-point statistics for turbulent boundary layers and channels at Reynolds numbers up to  $\delta^+ \approx 2000$ ,” *Phys. Fluids* **26**, 105109 (2014).
- <sup>37</sup> M. Gaster, E. Kit, and I. Wygnanski, “Large-scale structures in a forced turbulent mixing layer,” *J. Fluid Mech.* **150**, 23–39 (1985).